











Cite this: *J. Mater. Chem. A*, 2023, 11, 20549

# An argyrodite sulfide coated NCM cathode for improved interfacial contact in normal-pressure operational all-solid-state batteries†

Jun Tae Kim, <sup>ab</sup> Hyeon-Ji Shin, <sup>ac</sup> A-Yeon Kim, <sup>a</sup> Hyeonseong Oh,<sup>a</sup> Hun Kim, <sup>b</sup> Seungho Yu, <sup>a</sup> Hyoungchul Kim, <sup>d</sup> Kyung Yoon Chung, <sup>ac</sup> Jongsoo Kim, <sup>ef</sup> Yang-Kook Sun <sup>\*b</sup> and Hun-Gi Jung <sup>\*acef</sup>

The need for safe secondary power sources has generated significant interest in the development of all-solid-state batteries. Despite the development of solid electrolytes with excellent Li-ion conductivity, the challenges inherent to forming an intimate and stable interface between the cathode active material and the solid electrolyte limit the potential performance of all-solid-state batteries. Herein, we propose an efficient process by which a thin and uniform coating of layered oxide cathodes with sulfide solid electrolytes (argyrodite  $\text{Li}_6\text{PS}_5\text{Cl}$ ) may be obtained. The morphology of the coating agent with a thickness of approximately 30 nm and high uniformity is controlled by preparing  $\text{Li}_6\text{PS}_5\text{Cl}$  by one-pot synthesis. As a result, the material exhibits an excellent Li-ion conductivity of  $4.6 \text{ mS cm}^{-1}$  at a particle size of less than  $1 \mu\text{m}$ . The controlled argyrodite  $\text{Li}_6\text{PS}_5\text{Cl}$  was directly coated onto the  $\text{LiNi}_{0.5}\text{Co}_{0.2}\text{Mn}_{0.3}\text{O}_2$  cathode in an aprotic solvent environment. The coin-type all-solid-state cell developed using these argyrodite-coated cathode materials delivered a high discharge capacity of  $149.6 \text{ mA h g}^{-1}$  at 0.1C without additional external operating pressure during the charge–discharge process and retained 93.7% of its initial capacity after 100 cycles at 0.1C. It is revealed that the concrete contact between the  $\text{LiNi}_{0.5}\text{Co}_{0.2}\text{Mn}_{0.3}\text{O}_2$  cathode and  $\text{Li}_6\text{PS}_5\text{Cl}$  suppresses the cathode degradation reactions. The proposed method for coated cathode materials, which features the synthesis of controlled sulfide solid electrolyte materials and their simple coating process in the liquid-phase, can accelerate the development of all-solid-state batteries.

Received 2nd June 2023  
Accepted 3rd September 2023

DOI: 10.1039/d3ta03283c

rsc.li/materials-a

## 1. Introduction

Recent rapid increases in demand for rechargeable energy storage devices, especially in electric vehicles, mobile devices, and energy storage systems, have led to the application of lithium-ion batteries (LIBs) to various electronic devices, owing to their long lifetime and high power density.<sup>1–3</sup> However, LIBs

possess potential safety risks, especially due to the use of organic liquid electrolytes, which have high volatility and flammability. All-solid-state batteries (ASSBs) based on nonflammable solid electrolytes have been suggested as a solution to address these safety concerns. ASSBs can be operated under even high temperature conditions without the risk of ignition or explosion, and can achieve greater energy densities than LIBs.<sup>4,5</sup>

For decades, numerous studies have sought to enhance the Li-ion conductivity of various types of solid electrolytes, such as garnet, NASICON, and sulfide solid electrolytes, for effective application in ASSBs.<sup>6–11</sup> Among these options, sulfide solid electrolytes are particularly attractive by virtue of their impressive high Li-ion conductivity relative to that of liquid electrolytes. However, in contrast to conventional LIBs that use liquid electrolytes, where liquid electrolytes create a Li-ion conduction pathway throughout the electrode, Li-ion conduction between cathode materials and solid electrolytes is hindered due to solid–solid contact problems.<sup>12–14</sup> Consequently, the capacity of cathode materials and the Li-ion conducting ability of solid electrolytes cannot be fully utilized in ASSBs. Therefore, numerous recent studies have been conducted to create an

<sup>a</sup>Energy Storage Research Center, Korea Institution of Science and Technology, Seoul 02792, Republic of Korea. E-mail: hungi@kist.re.kr

<sup>b</sup>Department of Energy Engineering, Hanyang University, Seoul 04763, Republic of Korea. E-mail: yksun@hanyang.ac.kr

<sup>c</sup>Division of Energy and Environment Technology, KIST School, Korea University of Science and Technology, Seoul 02792, Republic of Korea

<sup>d</sup>Energy Materials Research Center, Korea Institution of Science and Technology, Seoul 02792, Republic of Korea

<sup>e</sup>KIST-SKKU Carbon-Neutral Research Center, Sungkyunkwan University, Suwon 16419, Republic of Korea

<sup>f</sup>Department of Energy Science, Sungkyunkwan University, Suwon 16419, Republic of Korea

† Electronic supplementary information (ESI) available: Voltage profile, BET analysis, Nyquist plots of LPSCl, SEM images, and X-ray photoelectron spectroscopy and impedance spectra. See DOI: <https://doi.org/10.1039/d3ta03283c>

intimate interfacial contact. Proposed approaches include electrode infiltration using liquid synthesis and solid electrolyte coating using pulsed laser deposition (PLD).<sup>13,15–17</sup> The liquid-phase process has been shown to be advantageous for uniformly coating solid electrolyte onto cathode materials; furthermore, it is widely applicable in industry. However, the solid electrolyte can undergo decomposition and crystal structure collapse depending on the solvent utilized, and the Li-ion conductivity of the solid electrolyte may still decrease despite solvent drying and thermal treatment.<sup>18–22</sup> Therefore, it is important to develop a liquid-phase process capable of mass production while maintaining the high Li-ion conductivity of solid electrolytes.

In this study, we developed an effective method for a thin and uniform coating layer of solid electrolytes on the surface of cathode active materials, based on the observation that the smaller particle among two particles with a large size difference is effectively adsorbed onto the surface of the larger particle in a suspension state.<sup>23</sup> A dispersant capable of reducing the particle size of the solid electrolyte was introduced into an aprotic mixing solvent to form a thin solid electrolyte coating layer, with a thickness of approximately 30 nm, on the surface of the cathode material.<sup>24–29</sup> Due to enhanced interfacial contact with the solid electrolyte, the  $\text{LiNi}_{0.5}\text{Co}_{0.2}\text{Mn}_{0.3}\text{O}_2$  (NCM523) cathode delivered a high discharge capacity of  $149.6 \text{ mA h g}^{-1}$ , which is 92.7% of the capacity attained when using a liquid electrolyte (Fig. S1†). Additionally, it was revealed that homogeneous electrochemical reactions induced by a uniform solid electrolyte coating layer effectively suppressed cathode degradation reactions, which are aggravated by uneven solid reactions. The developed liquid-phase thin coating process allows for efficient mass production in a shorter time than when using the solid phase ball-milling method.

## 2. Experimental methods

### Material preparation

**Ball-mill synthesis.**  $\text{Li}_6\text{PS}_5\text{Cl}$  was synthesized *via* a mechanochemical reaction. Stoichiometric mixtures of  $\text{Li}_2\text{S}$  (99.98%, Sigma-Aldrich),  $\text{P}_2\text{S}_5$  (99%, Sigma-Aldrich), and  $\text{LiCl}$  (99.98%, Sigma-Aldrich) were placed in a zirconia jar filled with zirconia balls and successively milled at 510 rpm for 20 h using a planetary ball-milling machine (Pulverisette6, Fritsch). The glass powders obtained were sealed in a quartz tube and annealed at  $550 \text{ }^\circ\text{C}$  for 5 h in a vacuum furnace to obtain crystalline  $\text{Li}_6\text{PS}_5\text{Cl}$  (denoted as LPSCl\_BM).

**Liquid-phase synthesis.**  $\text{Li}_6\text{PS}_5\text{Cl}$  was synthesized *via* a liquid-phase process with and without a dispersant. Stoichiometric mixtures of  $\text{Li}_2\text{S}$ ,  $\text{P}_2\text{S}_5$  and  $\text{LiCl}$  were used as raw materials. For liquid-phase synthesis, raw materials were added to the solvent (acetonitrile) and stirred vigorously at  $50 \text{ }^\circ\text{C}$ . In the case of liquid-phase synthesis using a dispersant, the solvent used in the synthesis was prepared by mixing acetonitrile and dibutyl ether (DBE) at a ratio of 8 : 2. Liquid-phase processes were carried out for 24 h. Following the reaction, the mixtures were dried at  $150 \text{ }^\circ\text{C}$  for 12 h under vacuum conditions, and then annealed under the same conditions as

described above to obtain  $\text{Li}_6\text{PS}_5\text{Cl}$  (denoted as LPSCl\_LP1 and LPSCl\_LP2).

**Coating process.** The  $\text{Li}_6\text{PS}_5\text{Cl}$ -coated NCM523 cathode was prepared using simple liquid-phase mixing with as-synthesized  $\text{Li}_6\text{PS}_5\text{Cl}$  powder and NCM523 cathode active material dispersed in acetonitrile. After mixing, the composite powder was dried at  $120 \text{ }^\circ\text{C}$  for 12 h under vacuum conditions. The resulting mass ratio of NCM523 to  $\text{Li}_6\text{PS}_5\text{Cl}$  in the coating layer was 95 : 5.

**Material characterization.** X-ray diffraction (XRD) measurements were conducted at a scan rate of  $1^\circ \text{ min}^{-1}$  over a  $2\theta$  range of  $10^\circ$  to  $90^\circ$  using a powder X-ray diffractometer (Miniflex II, Rigaku) with monochromatic  $\text{Cu K}_\alpha$  radiation ( $\lambda = 1.5406 \text{ \AA}$ ) at 30 kV. All powder samples were measured using an airtight holder to avoid air exposure. Raman spectra were acquired using a confocal Raman microscope (Renishaw Invia) equipped with a 532 nm laser. XPS (PHI 5000 VersaProbe, Ulvac-PHI) was performed using monochromated  $\text{Al K}_\alpha$  radiation ( $h\nu = 1486.6 \text{ eV}$ ). The X-ray spot size was  $100 \mu\text{m} \times 100 \mu\text{m}$ , and the narrow scan pass energy was set to 58.70 eV. The obtained binding energies were calibrated using the C 1s peak at 284.6 eV. Field emission scanning electron microscopy (FE-SEM) was performed using a Regulus 8230 (Hitachi, Tokyo) instrument equipped with an energy dispersive X-ray spectrometer (EDS, Ultimex, Oxford Instruments, United Kingdom). The samples were transferred using an airtight holder filled with Ar gas to reach the apparatus. A high-angle annular dark field scanning transmission electron microscope (HAADF-STEM, Talos, FEI Corp) equipped with an EDS (Super-X, Bruker) instrument was used to observe the morphologies of the cathode active material coated with sulfide solid electrolyte. To analyze the thickness of the solid electrolyte coating layer with line profiling, a focused ion beam (FIB, Helios NanoLab 600, FEI Corp) was used to cut a cross section of a particle. The size distributions of the synthesized  $\text{Li}_6\text{PS}_5\text{Cl}$  particles were measured using a laser diffraction particle size analyzer (ELSZ-100, Otsuka Electronics).

**Electrochemical characterization.** The ionic conductivity of SE was investigated using electrochemical impedance spectroscopy (EIS) measurements in the frequency range from 5 MHz to 100 Hz by applying a current amplitude of 100 mV (SI1260, Solartron). The blocking electrodes were prepared with a configuration of SS (stainless steel)/SE/SS using a 6 mm diameter polyarylether ether ketone (PEEK) mold. The activation energy ( $E_a$ ) was calculated from the Arrhenius plot of ionic conductivity measured at  $20 \text{ }^\circ\text{C}$  intervals in the range of room temperature to  $110 \text{ }^\circ\text{C}$ , and was maintained at the measurement temperature for 3 h to ensure thermal equilibrium. The electronic conductivity of SE was investigated using chronoamperometry (CA) measurements in the voltage range from 0.1 V to 0.5 V at 0.1 V intervals for 10 min. The composite cathode was prepared with NCM523,  $\text{Li}_6\text{PS}_5\text{Cl}$ , and vapor growth carbon fibers (VGCF, Showa Denko) in a weight ratio of 70 : 27 : 3 using a high-speed mixer (MM400, Retsch). A trilayer pellet for cell tests was fabricated by adding 150 mg of  $\text{Li}_6\text{PS}_5\text{Cl}$  SE powder to a 15 mm diameter mold and pressing at 370 MPa using a hydraulic press. Subsequently, 30 mg of the composite cathode was added and pressed at 410 MPa. Additionally,

100 mg of  $\text{Li}_{0.5}\text{In}$  alloy powder was spread and pressed at 190 MPa. The electrochemical performance of ASSBs was examined with a 2032-type coin cell using a battery cycler (BCS805, Biologic) in the voltage range of 2.0–3.6 V (vs.  $\text{Li}^+/\text{Li-In}$ ) at 30 °C. Galvanostatic cycling tests were conducted by applying a constant current–constant voltage (CC–CV) mode of charging and a constant current (CC) mode of discharging. The specific capacity was calculated using current rates of 0.1, 0.2, 0.5, and 1C based on the weight of active materials (1 C-rate = 180 mA  $\text{g}^{-1}$ ). EIS measurements of ASSB cells during cycling were performed over a range of 0.1 Hz to 1 MHz with an amplitude of 50 mV using an impedance analyzer (VMP3, Biologic). GITT measurements were carried out with a pulse of 0.5C for 60 s and 2 h rest. The contact between NCM523 and LPSCl particles ( $S$ ) was calculated according to the GITT measurement using eqn (1) as follows:

$$D = \frac{4}{\pi\tau} \left( \frac{m_{\text{NCM}} V_{\text{M}}}{M_{\text{NCM}} S} \right)^2 \left( \frac{\Delta E_{\text{s}}}{\Delta E_{\text{t}}} \right)^2 \quad (1)$$

where  $D$  is the chemical diffusion coefficient of NCM523,  $S$  is the contact area between cathode active material and solid electrolyte,  $\tau$  is the pulse duration,  $\Delta E_{\text{s}}$  is the steady-state voltage change,  $\Delta E_{\text{t}}$  is the transient voltage change,  $M_{\text{NCM}}$  is the molecular weight of the host,  $\text{Ni}_{0.5}\text{Co}_{0.2}\text{Mn}_{0.3}\text{O}_2$ ,  $m_{\text{NCM}}$  is the mass of the host in composite cathode, and  $V_{\text{M}}$  is the molar volume of the  $\text{LiNi}_{0.5}\text{Co}_{0.2}\text{Mn}_{0.3}\text{O}_2$  (20.29  $\text{cm}^3 \text{mol}^{-1}$ ).<sup>30,31</sup> The surface areas of NCM523 powders were obtained *via* Brunauer–Emmett–Teller (BET) analysis with  $\text{N}_2$  adsorption–desorption isotherm experiments (0.762  $\text{m}^2 \text{g}^{-1}$ ) (Fig. S2†).

### 3. Results and discussion

#### Morphology control of solid electrolyte as a coating agent

To reduce the particle size of solid electrolyte  $\text{Li}_6\text{PS}_5\text{Cl}$ , liquid-phase synthesis with a dispersant (LP2) was used. Dibutyl ether was adopted as the dispersant, since it is generally used for pulverization of the sulfide solid electrolyte and causes no side reaction with the sulfide solid electrolyte.<sup>32–34</sup> For comparison, the solid electrolyte was synthesized using a mechanochemical method with high-energy ball-milling (BM) and liquid-phase synthesis without a dispersant (LP1). Depending on the presence or absence of the dispersant, liquid-phase synthesis shows different aspects over time. In the case of liquid-phase synthesis without a dispersant, a mixture of  $\text{Li}_2\text{S}$ ,  $\text{P}_2\text{S}_5$ , and  $\text{LiCl}$  was separated into two layers within a few minutes (Fig. S3†). In accordance with the use of aprotic solvent, liquid-phase synthesis was conducted in a suspension, and layer separation occurred according to the agglomeration and size of the particles in the suspension.<sup>35,36</sup> Consequently, layer separation can be seen as precipitation by aggregation between reaction products, and a size difference of the solid electrolyte between liquid-phase synthesis with and without a dispersant can be inferred.<sup>37</sup> LPSCl prepared *via* liquid-phase synthesis with 20 wt% of DBE was successively characterized by X-ray diffraction (XRD) to ensure that the structure of LPSCl\_LP2 is well-organized. As shown in Fig. 1a, the XRD pattern of LPSCl\_LP2 showed a good match with the LPSCl

reference (PDF# 01-086-5500) without side products and precursor peaks corresponding to  $\text{Li}_2\text{S}$ ,  $\text{P}_2\text{S}_5$ , and  $\text{LiCl}$ . Additionally, the structure of LPSCl\_LP2 was analyzed using Raman spectroscopy (Fig. 1b). Similar to LPSCl\_LP1 and LPSCl\_BM, the spectra of LPSCl\_LP2 displayed a strong  $\text{PS}_4^{3-}$  polyanion peak centered at 421  $\text{cm}^{-1}$  without any other side peak. Based on the results of both characterization methods, LPSCl\_LP2 revealed similar structural properties to LPSCl synthesized by high-energy ball-milling and liquid-phase synthesis without a dispersant, indicating that the presence of the dispersant does not interrupt the formation of the argyrodite (LPSCl) structure. To confirm the effect of the dispersant on reducing the particle size, scanning electron microscopy (SEM) measurements were performed. LPSCl\_BM exhibited severe aggregation and showed a large particle size of around 10  $\mu\text{m}$  (Fig. 1c). In contrast to the solid electrolyte synthesized by high-energy ball-milling, LPSCl\_LP1 showed relatively low agglomeration and a particle size of approximately 4  $\mu\text{m}$  (Fig. 1d). In addition, LPSCl\_LP2 synthesized by liquid-phase synthesis with a dispersant (DBE) causes some agglomeration of small particles (with a size of 1  $\mu\text{m}$  or less) (Fig. 1e). By comparing SEM images of particles of each material, it was clearly demonstrated that the dispersant can be used to reduce the particle size of LPSCl by minimizing particle–particle interactions. Furthermore, particle size analysis (PSA) was performed to quantitatively examine the particle size distribution of the solid electrolyte. As shown in Fig. 1f, the average particle size values in the 50% cumulative population ( $D_{50}$ ) of LPSCl\_BM, LPSCl\_LP1, and LPSCl\_LP2 were 8.24, 3.01 and 1.44  $\mu\text{m}$ , respectively, indicating that the trend in SE particle size is consistent with SEM image observations. However, the measurements of the actual particle sizes of the solid electrolyte were difficult due to the formation of secondary particles as agglomerates, despite efforts to disperse the solid electrolyte particles in toluene. The ionic conductivity of the LPSCl samples was evaluated using the AC impedance method with symmetric SS/SE/SS cells after confirming the structural characterization and function of the dispersant. Nyquist plots are shown in Fig. S4†. Solid electrolytes synthesized using liquid-phase processes have ionic conductivities of 1  $\text{mS cm}^{-1}$  or less. The crystallinity of the solid electrolyte may vary as a function of annealing temperature, and solid electrolytes synthesized *via* liquid-phase synthesis may have high lithium ionic conductivities with high annealing temperatures.<sup>38</sup> The solid electrolytes obtained herein were annealed at a high temperature of 550 °C. The synthesized SE showed high lithium ionic conductivities of 4.7, 4.6, and 4.6  $\text{mS cm}^{-1}$  at room temperature with corresponding activation energies of 0.2498, 0.2360, and 0.2520 eV, respectively (Fig. 1g). When the annealing temperature was reduced to 180 °C, similar to previous reports, the lithium ionic conductivities of LPSCl\_BM, LPSCl\_LP1, and LPSCl\_LP2 decreased, as shown in Fig. S5.† The electronic conductivities of LPSCl samples were measured by a CA test at room temperature (Fig. S6†). As a result, it was confirmed that LPSCl\_BM, LPSCl\_LP1, and LPSCl\_LP2 have similar electronic conductivities of  $3.93 \times 10^{-9} \text{ S cm}^{-1}$ ,  $3.71 \times 10^{-9} \text{ S cm}^{-1}$ , and  $3.89 \times 10^{-9} \text{ S cm}^{-1}$ , respectively. This result is

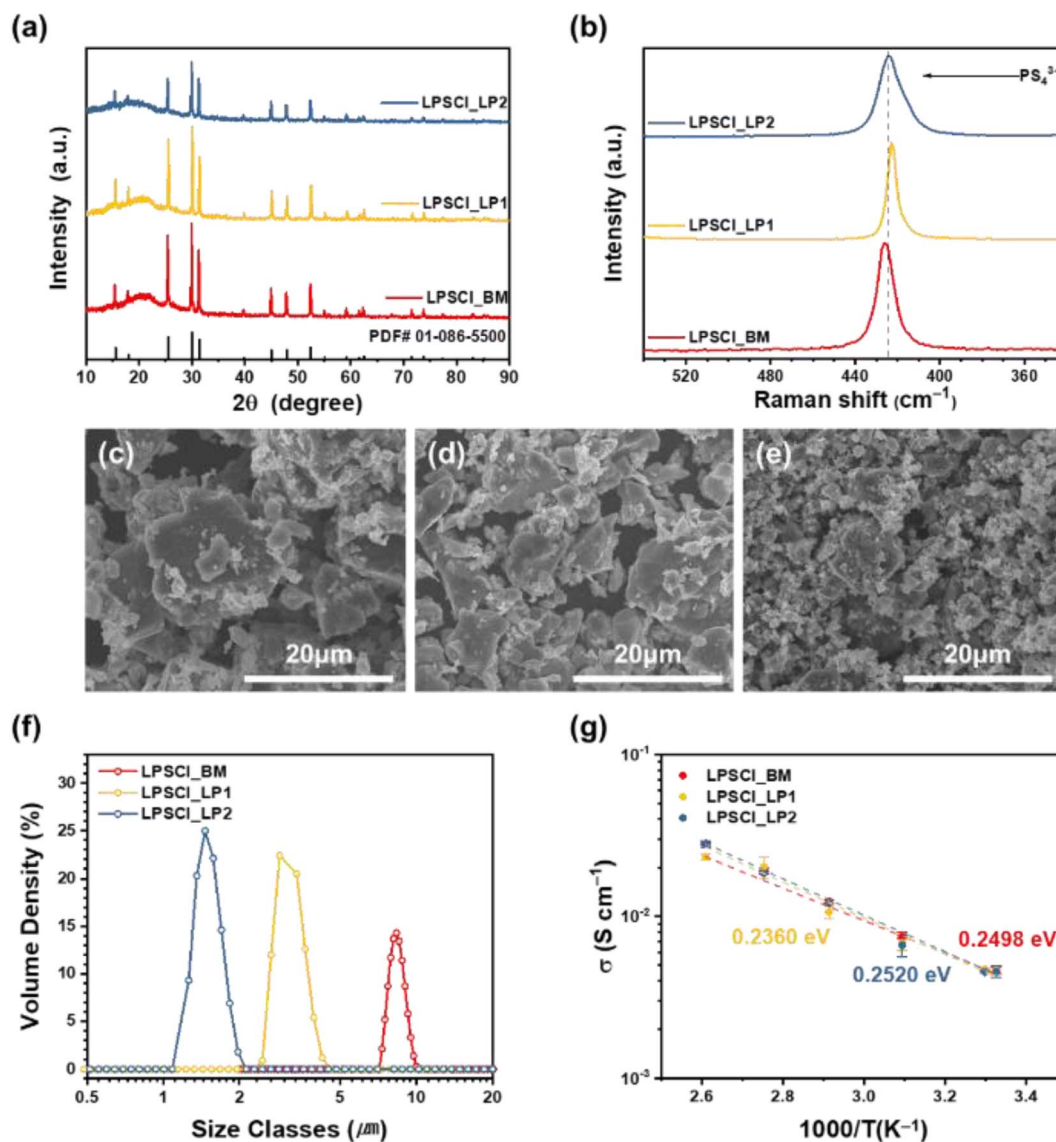


Fig. 1 Characterization of SE (Li<sub>6</sub>PS<sub>5</sub>Cl) synthesized by using a ball-mill, liquid-phase 1, and liquid-phase 2. (a) XRD patterns and (b) Raman spectra of SEs. SEM images of (c) LPSCI\_BM, (d) LPSCI\_LP1, and (e) LPSCI\_LP2. (f) Particle size distribution of LPSCI particles (obtained via different methods). (g) Arrhenius plots of lithium ionic conductivities for LPSCI\_BM, LPSCI\_LP1 and LPSCI\_LP2. Activation energy values are also shown.

attributed to no residual solvent carbonization even after the liquid-phase process.

### Solid electrolyte coating on the cathode

To elucidate the mechanism by which the particle size of the solid electrolyte enhanced the contact between the solid electrolyte and cathode active material within a composite cathode, LPSCI solid electrolyte prepared by various methods was coated on the surface of NCM523 (*via* a liquid-phase coating process). Cathode coating was performed by simply adding the cathode active material to the solid electrolyte suspension with acetonitrile, vigorously stirring the mixture, and vacuum drying at 120 °C (with a ratio of 95 : 5 wt% for NCM and LPSCI). Additional heat treatment was not applied due to the possibility of side reactions between NCM523 and the solid electrolyte.

Following the coating process, the NCM523 materials coated with solid electrolyte (denoted as NCM523\_BM, NCM523\_LP1, and NCM523\_LP2) were characterized using XRD. The XRD patterns of NCM523 coated with solid electrolyte were similar to that of bare NCM523, indicating that the cathode active material was preserved during the coating process (Fig. 2a). Furthermore, Raman spectroscopy was performed to confirm the presence of LPSCI on the surface of NCM523. As shown in Fig. 2b, a strong (PS<sub>4</sub><sup>3-</sup> polyanion) peak was detected on NCM523\_SE samples with a slight shift (~5 cm<sup>-1</sup>) to a lower wavelength region (red shift), which arises from the vibrational modes of PS<sub>4</sub><sup>3-</sup> due to the presence of other anions or the partial oxidation of the sulfide solid electrolyte due to surface reactions with the lithium transition metal oxide cathode.<sup>39-41</sup>

When the side reaction occurs, side reaction products, such as

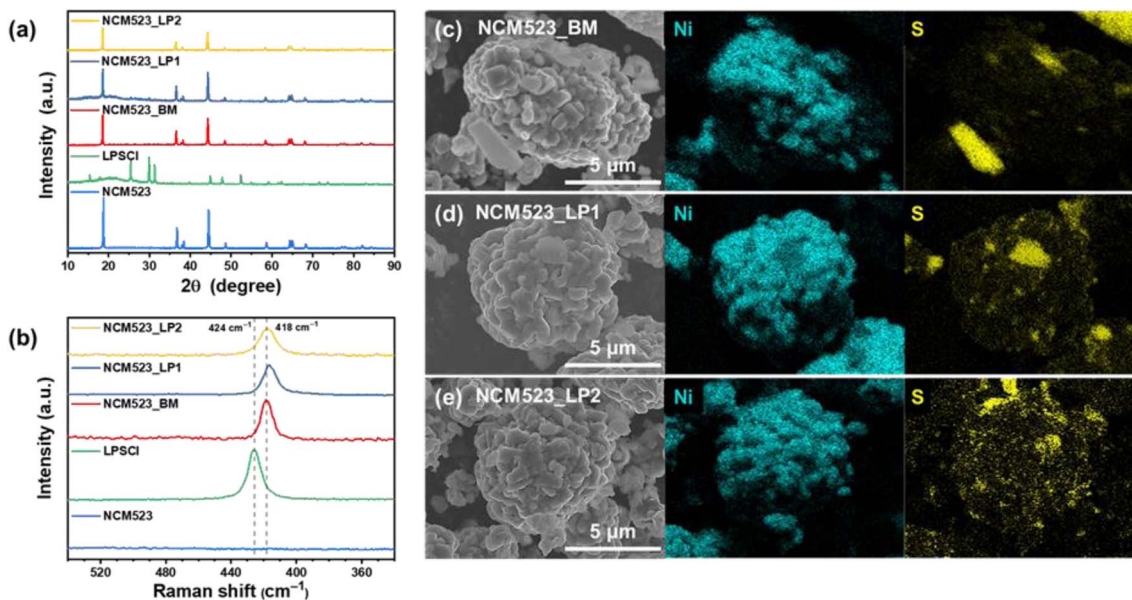


Fig. 2 Characterization of the cathode active material (NCM523) coated with LPSCI synthesized by BM and LP2. (a) XRD patterns and (b) Raman spectra of NCM523@SEs. SEM images of (c) NCM523\_BM, (d) NCM523\_LP1, and (e) NCM523\_LP2 with the corresponding EDS mapping of Ni, S, O, and P.

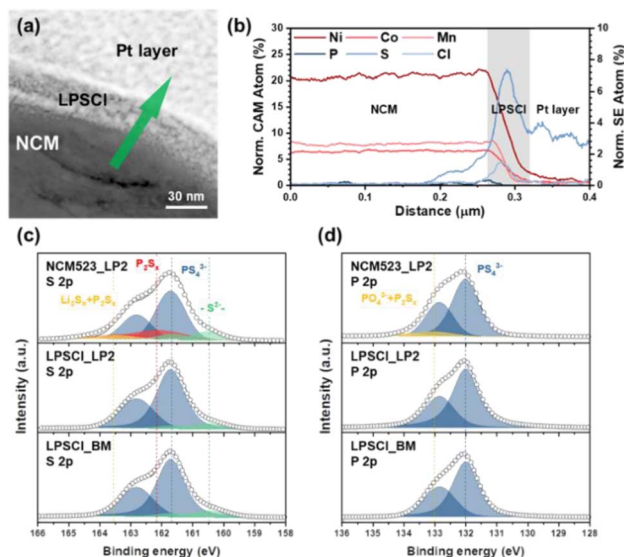


Fig. 3 Characterization of NCM523\_LP2. (a) HAADF-STEM image and (b) line profile of FIB cross-sectioned NCM523\_LP2. (c) S 2p and (d) P 2p XPS spectra of LPSCI\_BM, Li<sub>6</sub>PS<sub>5</sub>CLLP2, and NCM523\_LP2.

Li<sub>3</sub>PO<sub>4</sub>, are formed *via* the interfacial reaction, but at very low concentrations relative to that of the cathode active material and LPSCI. Consequently, it is difficult to observe a visible peak in the Raman spectra. After analyzing the stability of the cathode active material and the presence of solid electrolyte on the surface of the cathode active material following SE coating, the quality of the solid electrolyte coating layer was visualized using SEM and EDS analysis of Ni and S. As shown in Fig. 2c–e (Co, Mn, O, P, and Cl, Fig. S7<sup>†</sup>), the NCM523\_BM sample

revealed the formation of a nonuniform coating layer and the presence of large LPSCI particles attached to NCM523 due to their similar particle sizes. In the case of NCM523\_LP1, LPSCI\_LP1 had a relatively smaller particle size than LPSCI\_BM, resulting in a more even coating layer; however, EDS mapping confirmed the presence of LPSCI aggregates on the surface. In contrast, the NCM523\_LP2 sample exhibited a more uniform solid electrolyte coating layer with less agglomeration. In addition, the scale-up process shows the same pattern, and has the possibility of mass production (Fig. S8<sup>†</sup>). Consequently, it was determined that smaller particle sizes of solid electrolyte were advantageous for forming a uniform solid electrolyte coating layer. In addition, to evaluate the thickness of the solid electrolyte coating layer formed on the surface of the cathode active material, the NCM523\_LP2 sample with an evenly formed solid electrolyte coating layer was subjected to HAADF-STEM and line profile analyses after FIB cross sectional processing. As shown in Fig. 3a and b, HAADF-STEM analyses indicate that the sulfide solid electrolyte LPSCI\_LP2 is present between the cathode active material and Pt layer, confirming that a thin LPSCI coating layer of approximately 30 nm was formed through the corresponding line profile. The presence of the solid electrolyte coating layer on the surface of the cathode active material was confirmed through SEM imaging and line profile analysis; however, to identify the cause of the peak shift observed in the Raman spectra and the possible side reactions at the interface between the cathode active material and sulfide solid electrolyte, XPS analysis was conducted (Fig. 3c and d). LPSCI\_BM and LPSCI\_LP2 showed the same results for S 2p and P 2p spectra. The measured S 2p spectrum can be deconvoluted into four components. The dominant doublet of S 2p<sub>3/2</sub> at a binding energy of 161.7 eV represents the main peak of PS<sub>4</sub><sup>3-</sup>

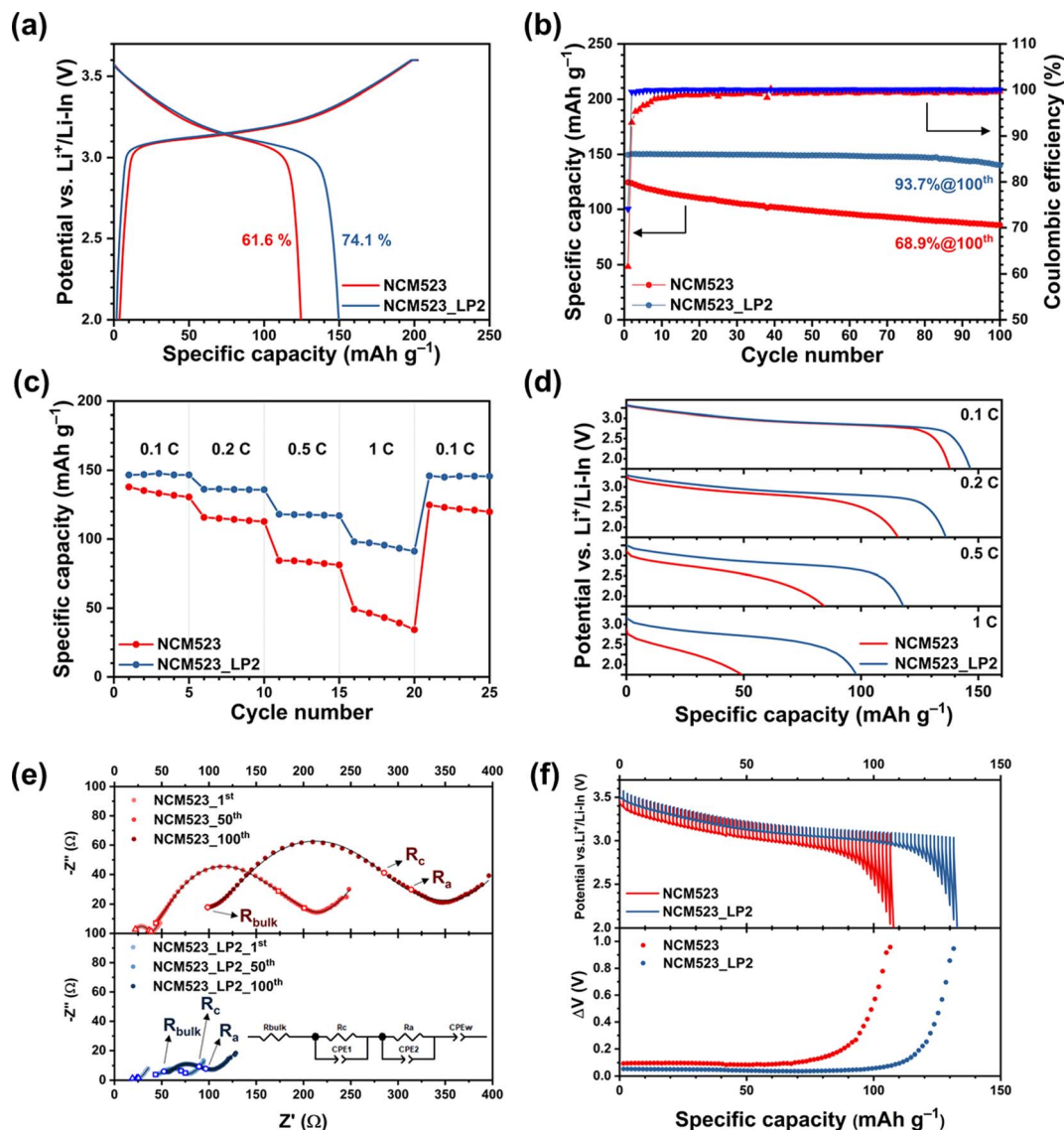


Fig. 4 Electrochemical characterization of all-solid-state cells employing bare NCM523 and NCM523\_LP2 at 30 °C. (a) 1st charge–discharge voltage profiles and (b) cycling performances at 0.1C. (c) Rate capabilities of all-solid-state cells featuring different composite cathodes. (d) Discharge–voltage profiles at different C-rates. (e) Electrochemical impedance spectra of all-solid-state cells after the 1st, 50th and 100th cycles. (f) Discharge–voltage profiles and corresponding polarization plots of cells obtained during the GITT. The polarization curves were plotted by subtracting the closed-circuit voltage (CCV) from the quasi-open-circuit voltage (QOCV) in the transient voltage profiles.

for argyrodite, and the small amount of S  $2p_{3/2}$  at a binding energy of 160.5 eV represents  $-S^{2-}$ . After SE coating of NCM523, two side peaks developed at 162.1 and 163.5 eV, corresponding to  $P_2S_x$  and  $Li_2S_n$ , respectively. Reactants with transition metals may also be included among the measured oxidized S species. In the P 2p spectrum, the major peak of  $2p_{3/2}$  for argyrodite is formed as a doublet at a binding energy of 132.0 eV without any other components. After SE coating, side products identified as oxidized P species ( $PO_xS_y$  and  $P_2S_x$ ) were observed at 133.0 eV, similar to the S 2p XPS results. Although side products may be naturally generated by contact with bare lithium transition metal oxide cathode active material and the sulfide solid electrolyte, changes in the Ni 2p spectrum were not observed (Fig. S9†).<sup>39–47</sup> Also, to confirm whether the phase of

the solid electrolyte was maintained after the solid electrolyte coating process, Rietveld refinement was carried out. As a result, it was confirmed that NCM523\_LP2 was composed of the cathode active material and the solid electrolyte in quantitative ratio of 95.9 : 4.1 wt%, respectively (Fig. S10†).

### Electrochemical performance

To evaluate the electrochemical performance of the composite cathode according to the formation of the solid electrolyte coating layer, NCM523\_LP2 was used to manufacture the composite cathode, which was then evaluated by galvanostatic cycling at 0.1C in the voltage range of 2.0–3.6 V versus  $Li^+/Li-In$ . Bare NCM523 was used under the same conditions for comparison. As shown in Fig. 4a, NCM523\_LP2 exhibited

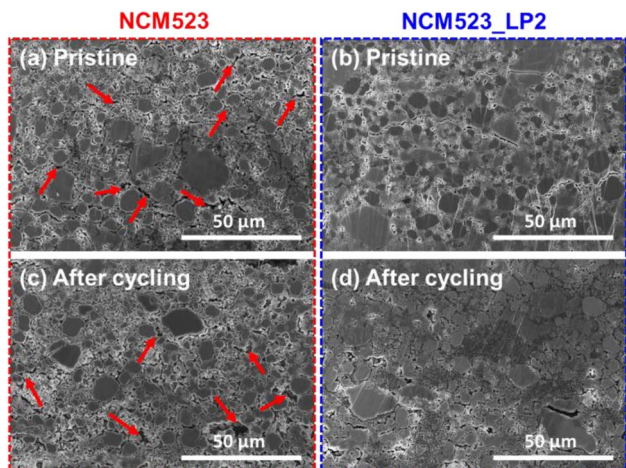


Fig. 5 Cross sectional SEM images of (a) and (c) composite cathodes prepared with bare NCM523 and (b) and (d) NCM523\_LP2 before cycling and after 100 cycles. Red arrows indicate void spaces.

a higher reversible discharge capacity of  $149.6 \text{ mA h g}^{-1}$  than bare NCM523 ( $124.5 \text{ mA h g}^{-1}$ ) with improved initial coulombic efficiency from 61.6 to 74.1% in the first charge–discharge profile. The other coated sample (NCM523\_LP1) was evaluated under the same conditions, but NCM523\_LP2 with a better solid electrolyte coating layer showed the best electrochemical performance and was chosen as the representative sample (Fig. S11†). In addition, cycling stability up to 100 cycles was significantly improved by solid electrolyte coating and the corresponding capacity retention increased from 68.9% to 93.7% (Fig. 4b). Furthermore, NCM523\_LP2 showed outstanding rate performance, exhibiting a specific capacity of  $146.6 \text{ mA h g}^{-1}$  at 0.1C and maintaining a retention ratio of 66.9% at 1C ( $98.0 \text{ mA h g}^{-1}$ ); in contrast, bare NCM523 showed a low specific capacity of  $137.8 \text{ mA h g}^{-1}$  and a retention ratio of 35.7% under the same conditions ( $49.3 \text{ mA h g}^{-1}$ ) (Fig. 4c). Moreover, when comparing the discharge curves of bare NCM523 and NCM523\_LP2 at different C-rates, the polarization in NCM523\_LP2 was shown to be significantly diminished (Fig. 4d). To investigate the reason for the improved electrochemical performance due to the solid electrolyte coating layer, electrochemical impedance spectroscopy was performed after reaching a fully charged state associated with the 1st, 50th, and 100th cycles (Fig. 4e). Although both the bare NCM523 and NCM523\_LP2 samples showed an increase in resistance associated with cycling, the increase in resistance of the bare NCM523 sample was much greater. This difference in electrochemical performance is likely due to the improved interfacial contact between the cathode active material and solid electrolyte in the composite cathode, resulting in the formation of a better lithium-ion pathway. To investigate this in detail, Nyquist plots were fitted with an equivalent circuit (R(RQ)(RQ)Q) as shown in the inset of Fig. 4e. The semicircle shown in the Nyquist plot can be divided into two regions, representing the interfaces between the cathode active material and solid electrolyte ( $R_c$ ) and between the anode and solid electrolyte ( $R_a$ ).  $R_c$

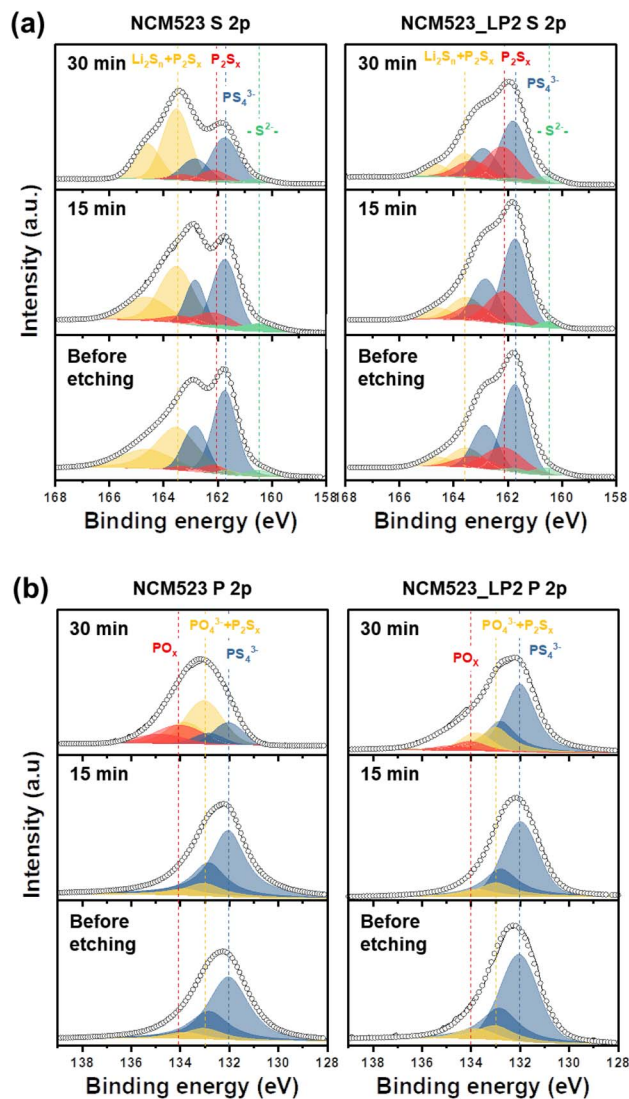


Fig. 6 Characterization of the composite cathode after 100 cycles. (a) S 2p and (b) P 2p XPS spectra of the composite cathode with bare NCM523 and NCM523\_LP2.

includes ionic transport within the composite cathode. To confirm the change in the resistance according to the formation of the solid electrolyte coating layer, their  $R_c$  values were compared. After the 1st charge, the  $R_c$  of NCM523\_LP2 showed a reduced resistance of  $4.79 \Omega$  compared to that of bare NCM523 ( $14.4 \Omega$ ) (the details of each resistance are shown in Fig. S12†), indicating an improvement in interfacial contact due to the solid electrolyte coating layer, which is related to the improvement observed in the initial discharge capacity. As cycling progressed, the increase in resistance at the interface between the cathode active material and the solid electrolyte in bare NCM523 became much greater than that in NCM523\_LP2. After the 50th and 100th cycles, NCM523\_LP2 had  $R_c$  values of  $25.51 \Omega$  and  $28.72 \Omega$ , respectively. The reduced resistance values can be explained by improved ion transfer, such that LPSCl\_LP2 particles with small sizes synthesized using the dispersant are very effective in forming smooth lithium ionic pathways in the

composite cathode. To calculate the interfacial contact area between the cathode active material and solid electrolyte, galvanostatic intermittent titration technique (GITT) measurements were performed, and the corresponding polarization curves were considered in relation to the decreased resistance (Fig. 4f). According to eqn (1), the relative active surface coverage of LPSCl for NCM523 on the NCM523\_LP2 electrode is 83.9%, which is approximately four times higher than that of the bare NCM523 electrode (19.7%). In addition, the polarization of NCM523\_LP2 during discharge is observed to be less than that of bare NCM52, depending on the difference in quasi-open-circuit voltage (QOCV). This is consistent with the electrochemical test results (Fig. 4d).

### Postmortem analysis

Based on the results of electrochemical performance testing, it can be inferred that the interfacial contact between the cathode active material and solid electrolyte is maintained before and after cycling; this was visually demonstrated using cross sectional SEM imaging (and corresponding EDS mapping) of the composite cathode after 100 cycles. Bare NCM523 shows multiple voids even in its pristine state, indicating loose interfacial contact (Fig. 5a). These multiple voids may vary depending on the fabrication pressure. The fabrication pressure has been diversified and compared; more pores were generated at a low fabrication pressure, and micro cracks were generated in the cathode active material at a high fabrication pressure. Therefore, the pressure of 410 MPa applied to pellet fabrication seems to be appropriate, and electrochemical performance also showed excellent results (Fig. S13†). On the other hand, the components of the composite cathode with NCM523\_LP2 were confirmed to form dense interfacial contacts (Fig. 5b). In addition, based on the results of sulfur EDS mapping, a band-shaped region was shown to form around the cathode active material (Fig. S14b†). Therefore, the initial electrochemical resistance and polarization were reduced, ensuring improved electrochemical performance. After 100 cycles, both composite cathodes showed the formation of pores compared to their pristine states. However, many areas in which the intimate contact between the cathode active material and solid electrolyte was maintained were observed despite the formation of pores due to volume changes in NCM through intercalation and deintercalation, especially in the case of NCM523\_LP2 (Fig. 5d). Numerous studies have reported chemical/electrochemical side reactions occurring between oxide cathode active materials and sulfide solid electrolytes. Additionally, Raman spectroscopy and XPS analyses of NCM523\_LP2 confirmed the formation of side reaction products, albeit in minute quantities, as shown in Fig. 2. To determine whether such side reaction products can contribute to stable operation by promoting a secure ionic pathway for homogeneous reaction sites through favorable interfacial contact, XPS analysis was conducted after 100 cycles. As part of the XPS measurements, depth profiling was performed to determine the uniformity of electrochemical reactions inside the electrodes. As shown in Fig. 6a, the S 2p spectra for both composite electrodes after 100 cycles show significantly

amplified ratios of oxidized species such as  $\text{Li}_2\text{S}_n$  and  $\text{P}_2\text{S}_x$  relative to the pristine state derived from the amount of side products generated from the contact (Fig. 3c and d). With increasing etching time (approaching from SE to NCM), the intensity of oxidized S species steadily increases, whereas the intensity of argyrodite ( $\text{PS}_4^{3-}$ ) weakens, indicating that major side reactions occur at the interface between the cathode active material and the solid electrolyte. In particular, for bare NCM523, the intensity of side product generation is stronger than that of argyrodite as it approaches the cathode active material. In contrast, for NCM523\_LP2, even after 30 minutes of etching, the intensity of the peak corresponding to argyrodite remains strong, indicating that the solid electrolyte coating layer can provide better electrochemical stability at the interface with less deterioration. In the P 2p spectrum, the overall tendency during depth profiling appears similar to that in the S 2p spectrum (Fig. 6b). Compared with the pristine state (Fig. 3d), the intensity of side products represented by  $\text{PO}_4^{3-}$  and  $\text{P}_2\text{S}_x$  increases at the surface of the cathode active material. Similar to the S 2p spectrum, the P 2p spectrum of bare NCM523 shows a larger amount of side products than that of the pristine state; even after 30 minutes of etching, additional side products corresponding to  $\text{PO}_x$  at a binding energy of 139.9 eV were observed. In contrast, for NCM523\_LP2, the number of side products containing  $\text{PO}_4^{3-}$ ,  $\text{P}_2\text{S}_x$ , and  $\text{PO}_x$  under the same conditions was relatively low. These results correspond well to the electrochemical properties.

## 4. Conclusions

In this study, a method for uniformly and thinly coating a sulfide solid electrolyte on the surface of a cathode material was demonstrated. We proposed a one-pot synthesis method for producing a solid electrolyte with superior ionic conductivity and small particle size and a method for coating it onto NCM particles in the liquid-phase. ASSBs featuring the NCM523 cathode showed excellent discharge capacity, rate capabilities, and capacity retention even without the application of additional external pressure. The homogeneous electrochemical reaction induced by the uniform coating suppressed parasitic reactions of the cathode. The proposed methods for synthesizing the solid electrolyte and coating the cathode material can be easily scaled up for mass production, thereby accelerating and broadening the practical use of ASSBs.

## Author contributions

J. T. Kim and H.-G. Jung conceived and designed the research. J. T. Kim, H.-J. Shin, A.-Y. Kim and H. Oh contributed to sample preparation, performed the experiments, and characterized the samples. S. Yu, H. Kim and K.-Y. Chung contributed to the interpretation of the results. J. T. Kim took the lead in writing the manuscript in consultation with H. Kim, Y.-K. Sun and H.-G. Jung. All the authors commented on and revised the manuscript.

## Conflicts of interest

There are no conflicts to declare.



## Acknowledgements

This research was supported by the Korea Institute of Science and Technology (KIST) institutional program (Project No. 2E32581); by the Technology Development Program to Solve Climate Changes of the National Research Foundation of Korea (NRF) funded by the Ministry of Science and ICT of Korea (No. 2022M3J1A1054151); by the Development Program of Core Industrial Technology funded by the Ministry of Trade, Industry and Energy of Korea (No. 20012318 and No. 20007045); and by the Institute of Civil Military Technology Cooperation funded by the Defense Acquisition Program Administration and Ministry of Trade, Industry and Energy of Korea (No. UM22213RD2).

## References

- N. Nitta, F. Wu, J. T. Lee and G. Yushin, *Mater. Today*, 2015, **18**, 252–264.
- Q. Zhao, S. Stalin, C.-Z. Zhao and L. A. Archer, *Nat. Rev. Mater.*, 2020, **5**, 229–252.
- J. Wu, S. Liu, F. Han, X. Yao and C. Wang, *Adv. Mater.*, 2021, **33**, 2000751.
- F. Duffner, N. Kronemeyer, J. Tübke, J. Leker, M. Winter and R. Schmich, *Nat. Energy*, 2021, **6**, 123–134.
- H.-D. Lim, J.-H. Park, H.-J. Shin, J. Jeong, J. T. Kim, K.-W. Nam, H.-G. Jung and K. Y. Chung, *Energy Storage Mater.*, 2020, **25**, 224–250.
- A. Kim, S. Woo, M. Kang, H. Park and B. Kang, *Front. Chem.*, 2020, **8**, 468.
- R. DeWees and H. Wang, *ChemSusChem*, 2019, **12**, 3713–3725.
- W. D. Jung, J.-S. Kim, S. Choi, S. Kim, M. Jeon, H.-G. Jung, K. Y. Chung, J.-H. Lee, B.-K. Kim, J.-H. Lee and H. Kim, *Nano Lett.*, 2020, **20**, 2303–2309.
- Y. Kato, S. Hori and R. Kanno, *Adv. Energy Mater.*, 2020, **10**, 2002153.
- Y. Lee, J. Jeong, H.-D. Lim, S.-O. Kim, H.-G. Jung, K. Y. Chung and S. Yu, *ACS Sustainable Chem. Eng.*, 2021, **9**, 120–128.
- Y. Lee, J. Jeong, H. J. Lee, M. Kim, D. Han, H. Kim, J. M. Yuk, K.-W. Nam, K. Y. Chung, H.-G. Jung and S. Yu, *ACS Energy Lett.*, 2022, **7**, 171–179.
- A. Sakuda, T. Takeuchi and H. Kobayashi, *Solid State Ionics*, 2016, **285**, 112–117.
- A. Sakuda, A. Hayashi and M. Tatsumisago, *Sci. Rep.*, 2013, **3**, 2261.
- B.-N. Yun, S. Lee, W. D. Jung, H.-J. Shin, J. T. Kim, S. Yu, K. Y. Chung, H. Kim and H.-G. Jung, *ACS Appl. Mater. Interfaces*, 2022, **14**, 9242–9248.
- D. H. Kim, D. Y. Oh, K. H. Park, Y. E. Choi, Y. J. Nam, H. A. Lee, S.-M. Lee and Y. S. Jung, *Nano Lett.*, 2017, **17**, 3013–3020.
- D. Y. Oh, D. H. Kim, S. H. Jung, J.-G. Han, N.-S. Choi and Y. S. Jung, *J. Mater. Chem. A*, 2017, **5**, 20771–20779.
- N. C. Rosero-Navarro, A. Miura and K. Tadanaga, *J. Power Sources*, 2018, **396**, 33–40.
- L. Zhou, K.-H. Park, X. Sun, F. Lalère, T. Adermann, P. Hartmann and L. F. Nazar, *ACS Energy Lett.*, 2019, **4**, 265–270.
- S. Teragawa, K. Aso, K. Tadanaga, A. Hayashi and M. Tatsumisago, *J. Mater. Chem. A*, 2014, **2**, 5095–5099.
- B. His Muhammad, S. Lee, J. T. Kim, H.-G. Jung, K. Y. Chung, D. Whang and H.-D. Lim, *Int. J. Energy Res.*, 2020, **44**, 11542–11549.
- N. H. H. Phuc, K. Morikawa, T. Mitsuhiro, H. Muto and A. Matsuda, *Ionics*, 2017, **23**, 2061–2067.
- Y. Nikodimos, C.-J. Huang, B. W. Taklu, W.-N. Su and B. J. Hwang, *Energy Environ. Sci.*, 2022, **15**, 991–1033.
- A. M. Islam, B. Z. Chowdhry and M. J. Snowden, *Adv. Colloid Interface Sci.*, 1995, **62**, 109–136.
- Q. Zhang, J. P. Mwizerwa, H. Wan, L. Cai, X. Xu and X. Yao, *J. Mater. Chem. A*, 2017, **5**, 23919–23925.
- X. Xu, Q. Ai, L. Pan, X. Ma, W. Zhai, Y. An, G. Hou, J. Chen, L. Zhang, P. Si, J. Lou, J. Feng and L. Ci, *Electrochim. Acta*, 2018, **276**, 325–332.
- J. Shi, G. Liu, W. Weng, L. Cai, Q. Zhang, J. Wu, X. Xu and X. Yao, *ACS Appl. Mater. Interfaces*, 2020, **12**, 14079–14086.
- L. Cai, H. Wan, Q. Zhang, J. P. Mwizerwa, X. Xu and X. Yao, *ACS Appl. Mater. Interfaces*, 2020, **12**, 33810–33816.
- M. Yang, Y. Yao, M. Chang, F. Tian, W. Xie, X. Zhao, Y. Yu and X. Yao, *Adv. Energy Mater.*, 2023, **13**, 2300962.
- H. Wan, L. Cai, F. Han, J. P. Mwizerwa, C. Wang and X. Yao, *Small*, 2019, **15**, 1905849.
- W. Hua, J. Zhang, Z. Zheng, W. Liu, X. Peng, X.-D. Guo, B. Zhong, Y.-J. Wang and X. Wang, *Dalton Trans.*, 2014, **43**, 14824–14832.
- K. M. Shaju, G. V. Subba Rao and B. V. R. Chowdari, *J. Electrochem. Soc.*, 2004, **151**, A1324.
- M. Cronau, M. Duchardt, M. Szabo and B. Roling, *Batteries Supercaps*, 2022, **5**, e202200041.
- C. Park, S. Lee, K. Kim, M. Kim, S. Choi and D. Shin, *J. Electrochem. Soc.*, 2019, **166**, A5318–A5322.
- S. Choi, S. Lee, J. Park, W. T. Nichols and D. Shin, *Appl. Surf. Sci.*, 2018, **444**, 10–14.
- A. Miura, N. C. Rosero-Navarro, A. Sakuda, K. Tadanaga, N. H. H. Phuc, A. Matsuda, N. Machida, A. Hayashi and M. Tatsumisago, *Nat. Rev. Chem*, 2019, **3**, 189–198.
- N. C. Rosero-Navarro, H. Niwa, A. Miura and K. Tadanaga, *Bol. Soc. Esp. Ceram. Vidrio*, 2023, **62**, 187–193.
- J. Gregory, *Adv. Colloid Interface Sci.*, 2009, **147–148**, 109–123.
- S. Yubuchi, H. Tsukasaki, A. Sakuda, S. Mori, A. Hayashi and M. Tatsumisago, *RSC Adv.*, 2019, **9**, 14465–14471.
- J. Zhang, C. Zheng, L. Li, Y. Xia, H. Huang, Y. Gan, C. Liang, X. He, X. Tao and W. Zhang, *Adv. Energy Mater.*, 2020, **10**, 1903311.
- W. D. Jung, M. Jeon, S. S. Shin, J.-S. Kim, H.-G. Jung, B.-K. Kim, J.-H. Lee, Y.-C. Chung and H. Kim, *ACS Omega*, 2020, **5**, 26015–26022.
- A. Banerjee, H. Tang, X. Wang, J.-H. Cheng, H. Nguyen, M. Zhang, D. H. S. Tan, T. A. Wynn, E. A. Wu, J.-M. Doux, T. Wu, L. Ma, G. E. Sterbinsky, M. S. D'Souza, S. P. Ong and Y. S. Meng, *ACS Appl. Mater. Interfaces*, 2019, **11**, 43138–43145.

- 42 J. Auvergniot, A. Cassel, D. Foix, V. Viallet, V. Seznec and R. Dedryvère, *Solid State Ionics*, 2017, **300**, 78–85.
- 43 J. Auvergniot, A. Cassel, J.-B. Ledeuil, V. Viallet, V. Seznec and R. Dedryvère, *Chem. Mater.*, 2017, **29**, 3883–3890.
- 44 R. Koerver, I. Ayyün, T. Leichtweiß, C. Dietrich, W. Zhang, J. O. Binder, P. Hartmann, W. G. Zeier and J. Janek, *Chem. Mater.*, 2017, **29**, 5574–5582.
- 45 D. H. S. Tan, E. A. Wu, H. Nguyen, Z. Chen, M. A. T. Marple, J.-M. Doux, X. Wang, H. Yang, A. Banerjee and Y. S. Meng, *ACS Energy Lett.*, 2019, **4**, 2418–2427.
- 46 F. Walther, R. Koerver, T. Fuchs, S. Ohno, J. Sann, M. Rohnke, W. G. Zeier and J. Janek, *Chem. Mater.*, 2019, **31**, 3745–3755.
- 47 F. Walther, S. Randau, Y. Schneider, J. Sann, M. Rohnke, F. H. Richter, W. G. Zeier and J. Janek, *Chem. Mater.*, 2020, **32**, 6123–6136.